

# Novel Issues in Reactionless Motion Control: Motion Analysis, Practical Task and Energy Consumption

Hiroki Sone, Dragomir Nenchev<sup>a</sup>

<sup>a</sup>*Department of Mechanical Systems Engineering, Graduate School of Engineering, Tokyo City University, 1-28-1, Tamazutsumi, Setagaya-ku, Tokyo, 158-8557, Japan*

---

## Abstract

This article addresses the following three issues in reactionless motion control: (i) motion analysis of reactionless control, (ii) proposal of a practical reactionless tasks and (iii) analysis of energy consumption under zero base attitude deviation. At the first issue, we analyze reactionless motion with a planar two-DoF model. A new feature is that the manipulator attachment position plays an important role as a bifurcation parameter. At the second issue, we aim to identify a practical task suitable for execution under reactionless motion control, with a typical type of a seven degree of freedom (DoF) redundant manipulator. With the manipulator model, the four-DoF reactionless motion can be used. We show a useful representation of its reactionless motion and propose inspection task using a hand camera based on a reactionless motion which consists of predominant wrist motion. We also mention the algorithmic singularity within the proposed reactionless task, and show that it can be relieved through the damped least-squares inverse with numerical filtering. Finally, we show an interesting character of reactionless motion. Under zero base attitude deviation, reactionless motion has highly equivalence to the instantaneous minimum energy optimization when reaction wheels are considered.

*Keywords:* Space robot, Reactionless motion control, Energy consumption

---

## 1. Introduction

Recently, development of space robots has been advanced to perform several complicated space missions, such as space debris removal, repairing and refueling for launched spacecrafts and construction of large space buildings [1]. For these missions, free-floating/flying space robots, which consists of

a satellite base, at least one manipulator arm and attitude control devices such as reaction wheels, has been proposed [2]. With this type of robots, the robot controller has to deal with the base rotation arising from the dynamic coupling between the manipulators and the floating satellite base [3]. Because of the base rotation, control methods which is used in terrestrial is not feasible, straightforwardly.

For this problem, the Generalized Jacobian, which includes the base motion effect evaluated from the momentum conservation law, was proposed [3, 4]. Through using this method, the end-effector velocities can be represented in terms of the joint velocity only. Hence, additional measurements of the base angular velocity/acceleration are not needed. The control methods for terrestrial robots can be used simply through replacing the Jacobian matrix with the generalized one. Based on this approach, some control and analysis methods have been developed [5, 6, 7]

On the other hand, the base rotation itself is a significant issue because it causes communication failure to the ground control center. In general, attitude control devices, such as reaction wheel, are employed to compensate the base attitude disturbances [8, 9]. However, it is known that the reaction wheel based method has limited capabilities w.r.t. the base attitude disturbances induced by the manipulator motion [10]. To avoid saturation of the reaction wheel signals, the manipulator has to be driven at very low speed. When some repeatable tasks, e.g. observation/inspection or assembly for construction missions, is performed, this low speed manipulation is not desirable from the perspective of work efficiency. Therefore, the dynamic coupling and reaction control of the manipulator are as important as its end-effector motion/force control.

As a pioneer work in reaction control of manipulators, the disturbance map was proposed for free-floating manipulator systems [11, 12]. With this method, the base disturbance can be visualized as a color map on the joint space. By using this tool, low reaction paths can be obtained through intuitive manner. However, if the system's degree of freedom (DoF) is more than two, it is difficult to apply this method.

On the other hand, a path planning method was proposed for zero reaction manipulation. This method is referred to as the Reaction Null-Space (RNS) method [13, 14], and provides a straightforward approach to reactionless motion generation. Therein, the condition for reactionless motion is derived from angular momentum conservation law. The method has been confirmed at on-orbit experiments with the Engineering Test Satellite VII

(ETS-VII) [15, 16].

In the previous studies, RNS-based reactionless motion controls have been considered [17, 18, 19]. For instance, the angular momentum distribution control for capturing non-cooperative satellites under the zero reaction condition was proposed [20]. It was investigated that the capability of reactionless motion control for debris removal task with a planar dual-arm system [21]. For vibration of flexible appendages on satellites, reactionless motion control was considered in addition to the vibration control [17]. In these studies, it can be seen that position control of the end-effector under reactionless control was focused on. However, it would be impossible in general type of manipulator models, e.g. six or seven-DoF manipulators, due to the limitation of kinematic structure. Indeed, the above methods were verified with two-dimensional models only. The possibility with spatial models is uncertain.

With spatial models, some interesting results were reported. With ETS-VII, simple reactionless tasks was proposed for the on-orbit experiment [15, 16]. In addition, verification with modified ETS-VII model adding an additional joint was presented. In this study, it was conclude that kinematically redundancy is important for extension of workspace under reactionless control. For point-to-point position control, the reaction-null/Jacobian transpose controller, which is obtained as the filtered version of the conventional transpose Jacobian controller, was proposed in [22]. This method was verified with a spatial serial/dual arm manipulator system with six-DoF manipulator. In that work, it was shown that a reachable region of the end-effector from an initial configuration is quite narrow due to the limitation of the kinematic structure. On the other hand, a singularity treatment method, which is called the Singularity Consistent Method [23], was applied for the algorithmic singularity of a minimum reaction control [23]. It was also confirmed that the workspace of the end-effector becomes quit narrow when considering the both constraints the manipulator and the base. In summary, we can conclude that position control of the end-effector under reactionless control is not appropriate in practical tasks even if singularity treatment techniques are used. However, despite the above disadvantages, reactionless motion control would be useful if we use it appropriately.

As a different matter, energy consumption has been considered in space systems. In the field of space robot, some reports can be found. For example, a control method which reduces energy consumption for free-flying space manipulators with redundant momentum-wheels was reported [24]. This

method is based on kinetic energy conservation throughout motion tasks. Energy optimum reactionless path planning for capturing tumbling satellite was also proposed in [25]. In this method, additional redundancy is used to optimize the kinetic energy of the manipulator. Also mechanical power was used as a cost function which is to be minimized for capturing non-cooperative satellites [26]. However, the energy consumption of reactionless motion itself, compared with reaction wheel based methods, is unclear so far.

In this work, according to the above background, we discuss the following two issues of reactionless motion control: (i) motion analysis of reactionless motion control, (ii) proposal of a practical reactionless task based on the results in [27] and (iii) analysis of energy consumption under reactionless motion control. Despite some studies based on reactionless motion have been considered, reactionless motion itself seems to be unclear. From the numerical analysis with a planar model, we show an interesting feature of reactionless motion: the manipulator attachment position plays an important role in addition to kinematically redundancy and it is a bifurcation parameter. At the second issue, we aim to identify a practical task suitable for execution under reactionless motion with a typical type of seven-DoF redundant manipulator model. From the empirical analysis, reactionless motion of the our manipulator model can be represented as superposition of the two specific motions: these are the predominant wrist motion and the elbow folding/unfolding motion. Among them, we focus on the predominant wrist motion to realize inspection missions using a hand camera. This mission is suitable for the predominant wrist motion because this task almost consists of the wrist motion. On energy consumption of reactionless motion, we show that reactionless motion is almost equivalent to the instantaneous minimum energy motion under zero base-attitude deviation. To estimate energy reduction, we compare the energy consumption in the above practical task with the inverse Jacobian controller.

This paper is organized as follows. In the following section we describe the momentum conservation law and the Reaction Null Space projection. In addition, a brief review of the character of reactionless motion control is described with a planar manipulator model. In Section 4, we describes the our manipulator model and provide a useful representation of its reactionless motion. Based on its reactionless motion, we propose inspection task using a hand camera under reactionless motion control. Numerical simulations show capabilities of the proposed method, with comparison to the inverse Jacobian controller. Finally, energy consumption of reactionless motion control

is discussed in Section 6 and then the paper will be summarized in Section 7.

## 2. A brief review of reactionless motion control

### 2.1. Angular momentum conservation law

We consider a free-flying space robot model consisting of a satellite base and a serial manipulator arm of  $n$ -DoF. In space environment, it is known that linear and angular momenta are conserved when there is no external force. Actually, the gravity gradient torque and solar radiation force violate this conservation. However, since the duration time of space robot missions is relatively short, we can assume that the momenta are conserved.

The conservation law of momenta is expressed as follows [20]:

$$\begin{bmatrix} \mathbf{p} \\ \mathbf{l}_b \end{bmatrix} = \begin{bmatrix} \mathbf{M}_v & \mathbf{M}_{vw} \\ \mathbf{M}_{vw} & \mathbf{M}_\omega \end{bmatrix} \begin{bmatrix} \mathbf{v}_b \\ \boldsymbol{\omega}_b \end{bmatrix} + \begin{bmatrix} \mathbf{M}_{vm} \\ \mathbf{M}_{\omega m} \end{bmatrix} \dot{\boldsymbol{\theta}} + \begin{bmatrix} \mathbf{M}_{vr} \\ \mathbf{M}_{\omega r} \end{bmatrix} \dot{\boldsymbol{\phi}} + \begin{bmatrix} \mathbf{0} \\ \mathbf{r}_{bc} \times \mathbf{p} \end{bmatrix} \quad (1)$$

where,  $\mathbf{p}$ ,  $\mathbf{l}_b \in \mathbb{R}^3$  denote constant linear and angular momentum w.r.t. the center of mass (CoM) of the base,  $\mathbf{v}_b$ ,  $\boldsymbol{\omega}_b \in \mathbb{R}^3$  stand for linear and angular velocity of the base, and  $\dot{\boldsymbol{\theta}} \in \mathbb{R}^n$  and  $\dot{\boldsymbol{\phi}} \in \mathbb{R}^3$  are the joint velocity and the reaction wheel velocity vector, respectively.  $\mathbf{M}_v$ ,  $\mathbf{M}_{vw}$ ,  $\mathbf{M}_\omega \in \mathbb{R}^{3 \times 3}$  are submatrices of the composite-rigid-body (CRB) inertia matrix,  $\mathbf{M}_{vm}$ ,  $\mathbf{M}_{\omega m} \in \mathbb{R}^{3 \times n}$  denote inertia submatrices related to the dynamic coupling between the base and the manipulator.  $\mathbf{M}_{vr}$ ,  $\mathbf{M}_{\omega r} \in \mathbb{R}^{3 \times 3}$  denote inertia matrices related to the dynamic coupling between the base and the reaction wheels. Note that  $\mathbf{M}_{vm}$  and  $\mathbf{M}_{\omega m}$  are referred to as the *coupling inertia matrix* [28].  $\mathbf{r}_{bc} \in \mathbb{R}^3$  is the position vector of the base w.r.t. the whole system's CoM.

For free-flying space manipulators, the angular momentum conservation law, especially, is of primary importance. Indeed, it has been noted that even slight variations of the base attitude may cause a failure in the communication between the robot and the ground control center. The angular momentum conservation law can be written in the following form with zero initial momentum [20]:

$$\tilde{\mathbf{M}}_\omega \boldsymbol{\omega}_b + \tilde{\mathbf{M}}_{\omega m} \dot{\boldsymbol{\theta}} + \tilde{\mathbf{M}}_{\omega r} \dot{\boldsymbol{\phi}} = \mathbf{0} \quad (2)$$

where, the notation  $(\tilde{\circ})$  represents a quantity that includes the base linear motion effect:  $\tilde{\mathbf{M}}_\omega = \mathbf{M}_\omega - \mathbf{M}_{vw}^T \mathbf{M}_v^{-1} \mathbf{M}_{vw}$ ,  $\tilde{\mathbf{M}}_{\omega m} = \mathbf{M}_{\omega m} - \mathbf{M}_{vw}^T \mathbf{M}_v^{-1} \mathbf{M}_{vm}$  and  $\tilde{\mathbf{M}}_{\omega r} = \mathbf{M}_{\omega r}$ . In the above equation, the first term on the r.h.s. is the partial angular momentum stemming from base rotation, the second

term, on the other hand, results from manipulator motion; it represents the base disturbance in terms of velocity. The term is referred to as the *coupling angular momentum* [28]. Finally, the third term represents the angular momentum stored in the reaction wheels. We regard the system is as a free-floating system ( $\dot{\boldsymbol{\phi}} = \mathbf{0}$ ) until Section 6. For the sake of simplicity, zero initial momenta are assumed without losing generality, hereafter.

## 2.2. Reaction Null-Space

Reactionless motions are variations of the manipulator configuration that conserve a zero initial base angular momentum throughout the entire motion. This implies  $\boldsymbol{\omega}_b = \mathbf{0}$ , and hence,

$$\tilde{\mathbf{M}}_{\omega m} \dot{\boldsymbol{\theta}} = \mathbf{0}. \quad (3)$$

From this equation, the set of reactionless motion can be represented as [14]:

$$\dot{\boldsymbol{\theta}} = \mathbf{P}_{RNS} \dot{\boldsymbol{\theta}}_a, \quad (4)$$

where,  $\mathbf{P}_{RNS} (= \mathbf{E} - \tilde{\mathbf{M}}_{\omega m}^+ \tilde{\mathbf{M}}_{\omega m}) \in \mathbb{R}^{n \times n}$  denotes a projector onto the null-space of the coupling inertia matrix,  $\mathbf{E} \in \mathbb{R}^{n \times n}$  is the identity matrix and  $(\circ)^+$  stands for the pseudoinverse matrix.  $\dot{\boldsymbol{\theta}}_a \in \mathbb{R}^n$  is an arbitrary vector with the dimensions of joint velocity. It plays the role of a vector-parameter for the set of reactionless motions. It is apparent that the null-space of the coupling inertia matrix, referred henceforth as the *Reaction Null-Space* (RNS), plays an important role for reactionless motion generation. Here, it should be noted that all of reactionless motions can be represented in the above notation. Hence, the zero reaction motions generated by other methods, e.g. nonlinear optimization programming and so on, are basically same as that of (4).

## 3. Qualitative analysis on reactionless motion control with a planar model

### 3.1. Vector field of reactionless motion

Despite there are some results based on reactionless motion control, the characters of reactionless motion have not been mentioned in pre-reported results. Here, we describe some details of reactionless motion with a planar model.

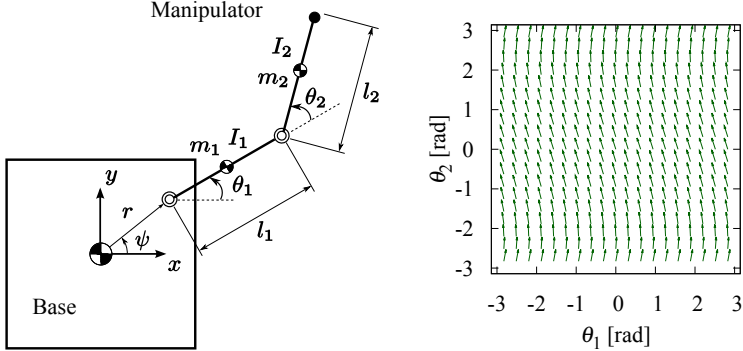


Figure 1: A planar two-DoF space manipulator model with  $m_i = 100$  kg,  $l_i = 1.0$  m ( $i = 1, 2$ ); the base mass is  $m_b = 1000$  kg. The vector field is obtain with  $r = 0$  m.

We consider a planar two-DoF manipulator as shown in Fig. 1. This model is the most simplest model which can generate reactionless motion. Reactionless motion with this model can be represented as follows:

$$\dot{\boldsymbol{\theta}} = b\mathbf{n}(\boldsymbol{\theta}) \quad (5)$$

where,  $\mathbf{n}(\boldsymbol{\theta}) \in \mathbb{R}^2$  is the null-space vector of the coupling inertia matrix,  $b$  is an arbitrary scalar.  $\mathbf{n}(\boldsymbol{\theta})$  can be uniquely obtained through appropriate methods, i.e. Singular Value Decomposition (SVD) or co-factor method. We assume that  $\mathbf{n}(\boldsymbol{\theta})$  is already normalized, and  $b$  is a time-independent constant scalar, for the sake of simplicity. Hence, (5) can be regarded as an autonomous nonlinear system. The right hand side in (5) defines the vector field of reactionless motion on the joint space.

We examine the characters of reactionless motion with vector field of the above system. For the sake of simplicity, we assume that the manipulator is attached on the CoM of the base. The masses are  $m_b = 1000$  kg,  $m_1 = m_2 = 100$  kg, and the link length are  $l_1 = l_2 = 1.0$  m, respectively. Then, the vector field is depicted in Fig. 1.

Because the manipulator is attached symmetrically, the vector field has rotational symmetry w.r.t. joint 1. As an important character, we can see that the reactionless motion is almost composed of the motion of joint 2. Because reactionless motion is a motion which conserves the angular momentum to zero (or constant), joints which induce a large angular momentum cannot move widely. With this model, the angular momentum induced by the joint 1 motion must be larger than that of the joint 2 motion due to the large

inertia moment and the long moment arm. As a result, the above mentioned character is observed.

### 3.2. Fixed point and bifurcation

In the above case, the system does not have fixed points. However, with variation of a specific parameter, we can observe occurrence of bifurcation in reactionless motion. This bifurcation phenomenon is largely related to the manipulator attachment position. The attachment position is defined as follows:

$$\begin{bmatrix} x_a \\ y_a \end{bmatrix} = r \begin{bmatrix} \cos \psi \\ \sin \psi \end{bmatrix} \quad (6)$$

where,  $(\circ)_a$  is the coordinate of the attachment position,  $r$  is the distance between the attachment position and the base CoM,  $\psi$  is the angle as shown in Fig. 1. Among these parameters,  $r$  plays an important role as a *bifurcation parameter* in this system. Note that we assume  $\psi = 0$  rad because this parameter does not influence the topological structure in the system due to rotational symmetry of mechanics. The condition  $\psi = 0$  rad means the manipulator attachment position varies along  $x$ -axis of the base frame.

We show the vector field and nullclines with several values of  $r$  in Fig. 2. In the figures, the upper part represents the vector field and the lower part depicts nullclines for each joint direction: lines in red are nullcline for joint 1, lines in blue are that for joint 2. When  $r = 0.5$  m, we can see that there is no fixed point, because the motion of joint 2 never stops at any points in joint space. On the other hand, occurrence of the bifurcation can be observed when  $r \approx 0.945$  m. Then, two fixed point are created at intersection points of two nullclines. Increasing the bifurcation parameter, the fixed points which were created at same point are gradually separated each other ( $r = 1.5$  m). Finally, when  $r \rightarrow \infty$  two of the fixed points converge to  $\theta_2 \rightarrow 0$  rad and the others are to be  $\theta_2 \rightarrow \pm\pi$  rad, respectively.

### 3.3. The singularities within the coupling inertia matrix

In above discussion, we showed the existence of the fixed point of reactionless motion control. This is related to the singularities of the coupling inertia matrix. In contrast to kinematic singularities, the singularities of the coupling inertia matrix have not been discussed, so far. We provide an insight of this singularity with the planar model mentioned above.

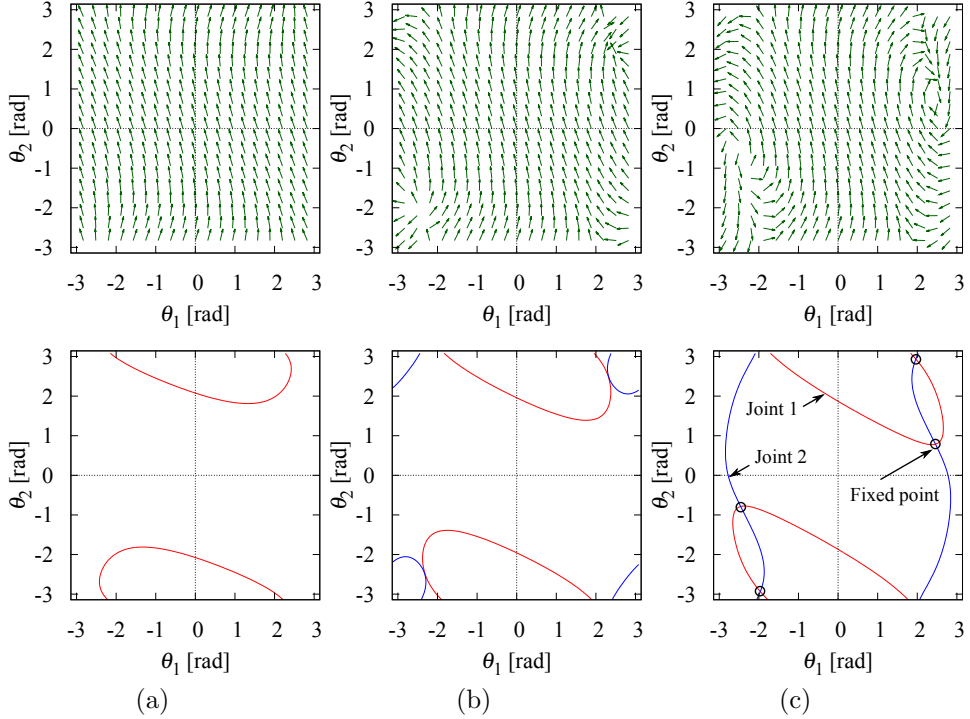


Figure 2: The vector field and nullclines for each joint direction with variation  $r$ : (a)  $r = 0.5$  m, (b)  $r = 0.945$  m and (c)  $r = 1.5$  m.

We show the determinant of the coupling inertia matrix with  $r = 1.5$  m as a color map in Fig. 3 (a). In the color map, the determinant takes large values in bright areas, while the most dark area represents the singularity. We can see that the determinant takes its maximum value at  $\boldsymbol{\theta} = [0 \ 0]^T$  rad. This is an extended configuration and the manipulator CoM is located on the farthest away from the base CoM with this configuration. The determinant of the coupling inertia matrix can be discussed associated with the distance between the manipulator CoM and the base one, because the distance determines the amplitude of the coupling angular momentum. The distance on the joint space is depicted in Fig. 3 (b). With comparison to these maps, it can be seen that the determinant takes large values when the distance is long: there is no fixed point within the location where the CoM distance becomes large. In the case of spatial models, the direction of each joint axis become significant, in addition to this character.

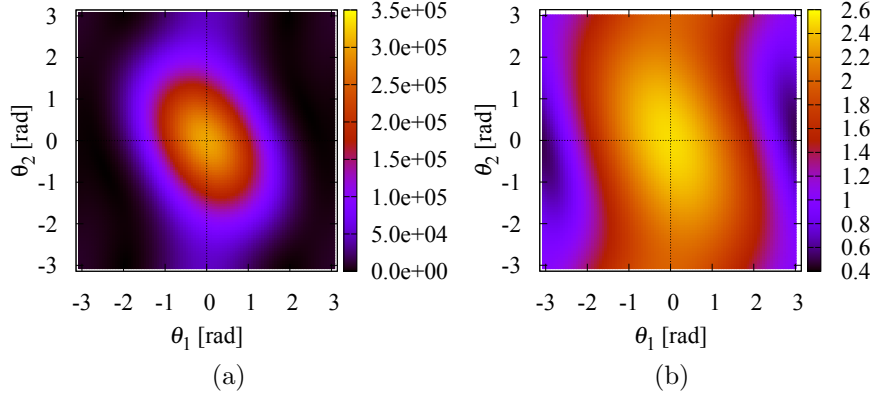


Figure 3: This figure shows the determinant of the coupling inertia matrix and the distance between the manipulator CoM and the base one as color map: (a)  $\det(\tilde{M}_{\omega m} \tilde{M}_{\omega m}^T)$  and (b) the distance between the manipulator CoM and the base one.

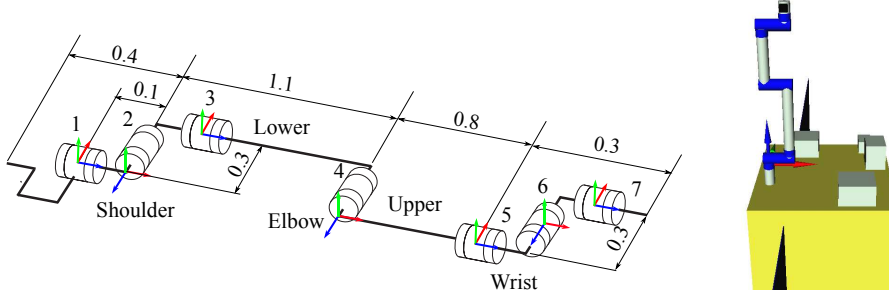


Figure 4: Our manipulator model with seven-DoF mechanism at the initial configuration ( $\theta_i = 0$  rad,  $\forall \theta_i$ ).

#### 4. Reactionless inspection task using a hand camera

In this section, we will introduce a practical task suitable for execution under reactionless motion control with a spatial redundant manipulator. First, we describe the manipulator model and its reactionless motion. Then, the task description and the control command will be mentioned. Finally, we verify the performance of the proposed reactionless task compared with a conventional kinematic controller.

##### 4.1. Manipulator model and its reactionless motion

In this study, we consider a free-flying space robot model consisting of a satellite base, a serial seven-DoF redundant manipulator. The manipulator

Table 1: Dynamic model parameters

	Mass [kg]	Inertia moment [kgm <sup>2</sup> ]		
<i>i</i>	$m_i$	$I_{xi}$	$I_{yi}$	$I_{zi}$
<i>b</i>	2552	6200	3540	7090
1	30.0	0.0671	0.0671	0.0851
2	30.0	0.0843	0.267	0.267
3	45.0	3.81	3.81	0.127
4	40.0	0.113	2.19	2.19
5	20.0	0.213	0.213	0.0250
6	20.0	0.0250	0.0292	0.0292
7	25.0	0.0990	0.0990	0.0313

is characterized by a kinematic chain with a distinctive lower/upper arm sub-chain, including a rotational “elbow” joint and “shoulder” and “wrist” joints with offsets. The kinematic structure and simulation model are displayed in Fig. 4. The manipulator attachment position are designed based on that of ETS-VII as  $[-0.79 \ -0.29 \ 1.0]^T$  m with respect to the base CoM [10]. The dynamic model parameters are shown in Tab. 1.

Before proceeding with the proposal of practical reactionless motion task, we have to identify reactionless motion with the manipulator model. In this model, the DoF of reactionless motion is four, which is obtained as the difference between the joint number and the base attitude DoF (three). The following discussion provides a useful representation of the four-DoF motion.

First, we divide the kinematic structure into the positioning and the wrist subchains for practical aspect. The positioning subchain consists of Joint 1 through 4. The rest of joints constitute the wrist subchain.

Here, we focus on the amplitude of the angular momentum produced by each subchain. Because of small mass and the length of moment arm, we can regard that the angular momentum produced by the motion of wrist subchain is far smaller than these of the positioning subchain. Hence, it can be considered that the positioning subchain can compensate the base disturbance induced by the wrist subchain motion, completely. In other words, a part of the reactionless motion consists of free wrist subchain motions and small positioning subchain motions as shown in Fig. 5 (a). This motion is three-DoF reactionless motion and is defined as the predominant wrist motion,

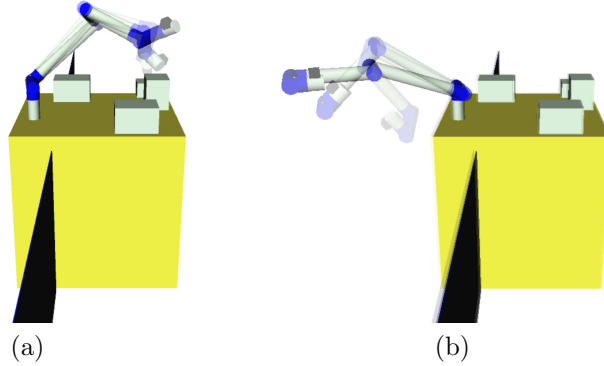


Figure 5: Reactionless motion of the manipulator model: (a) the predominant wrist motion and (b) the elbow folding motion.

hereafter.

The remaining one-DoF reactionless motion is uniquely determined as the null-space of the submatrix of the coupling inertia matrix related to the positioning subchain part. This motion approximately consists of the elbow folding/unfolding motion as shown in Fig. 5 (b). From angular momentum conservation, we can assume that the motion of Joint 1 and 2 are relatively small in the above two motions. Since these two motion are mathematically orthogonal, the reactionless motion of the our manipulator model can be represented as the superposition of these motions.

From the above analysis, we can obtain the following fact: because the end-effector position largely depends on the motion of the positioning sub-chain, the DoF of the end-effector position control under reactionless motion is approximately 1 according to that of the positioning subchain. Namely, even if the system has enough DoF, position control under reactionless motion is not feasible due to the limitation of the kinematic structure. From the reason, we focus on the end-effector orientation control with the predominant wrist motion rather than considering the position control. This makes our research different from the previous studies.

#### 4.2. Reactionless inspection task

##### 4.2.1. Task definition

One frequent task for free-floating space robots is inspection with a hand camera for various devices mounted on own satellite, large space structures or satellites to be serviced, as shown in Fig. 6. Such task was also performed

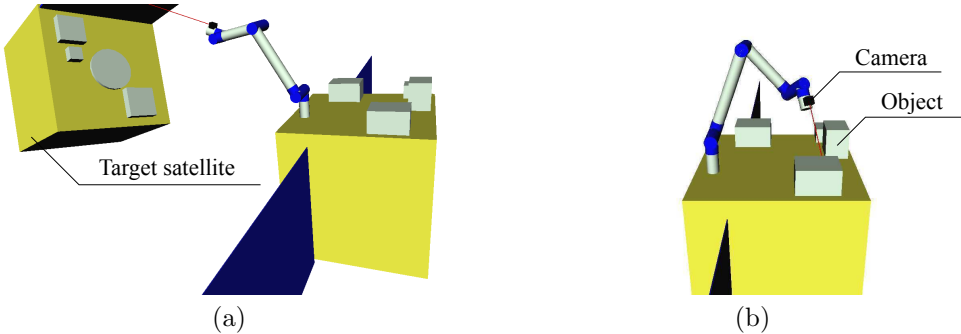


Figure 6: Inspection task using the hand camera: (a) target satellite to be refueled or captured and (b) own-satellite attached devices.

within the ETS-VII mission [29] without using reactionless control. At this motion task, once the arm is positioned appropriately, the camera view angle for inspection is changed by rotating the wrist. This task would be expected to perform several times in almost all kind of missions, such as construction, maintenance, debris removal and so on. Hence, this task is a good candidate for execution under reactionless motion control to reduce work efficiency.

We consider the following three tasks in order to accomplish the camera inspection.

1. Reactionless constraint of the base attitude (three-DoF)
2. Orientation control of the end-effector (three-DoF)
3. Stabilization of the wrist position

The third one is due to the following reason: a large deflection of the wrist might induce a collision problem and camera view changes.

The above tasks are simultaneously realized through the theory of task priority [30]. In this theory, the tasks are assigned the priorities according to its relative importance. The highest priority task, which is called the *primary task*, can be accomplished without the effect from lower priority tasks. Hence, lower priority tasks must be designed not to disturb the higher priority tasks. In order to ensure the prioritization, lower priority tasks are projected to the null-space of all-higher priority tasks. We make a control command according to this theory.

#### 4.2.2. Control command

We regard the reactionless constraint as the primary task, the end-effector orientation control is the second one and the wrist position stabilization is

the third one. The control command of the joint velocity, considering the above priorities, can be obtained as follows:

$$\dot{\boldsymbol{\theta}}^{ref} = {}^e\bar{\mathbf{J}}_{\omega}^+ \boldsymbol{\omega}_e^{ref} + k_g \mathbf{P}^w \mathbf{J}_v^T \Delta \mathbf{p}_w \quad (7)$$

where,  $\boldsymbol{\omega}_e \in \mathbb{R}^3$  is angular velocity of the end-effector,  ${}^e\bar{\mathbf{J}}_{\omega} = [{}^e\mathbf{J}_{\omega} \mathbf{P}_{RNS}] \in \mathbb{R}^{3 \times 7}$  is the restricted Jacobian matrix,  ${}^e\mathbf{J}_{\omega}$  and  ${}^w\mathbf{J}_v \in \mathbb{R}^{3 \times 7}$  stand for the Jacobian w.r.t. the angular velocity of the end-effector and wrist linear velocity. Superscripts explain the specific point associated with the velocities. Note that the superscript of the end-effector  ${}^e(\circ)$  will be ignored for description convenience, hereafter.  $\mathbf{P} = \mathbf{P}_{RNS}(\mathbf{E} - \bar{\mathbf{J}}_{\omega}^+ \bar{\mathbf{J}}_{\omega})$  projects an arbitrary vector onto the null-space of the base and the end-effector tasks [31].  $\Delta \mathbf{p}_w (= \mathbf{p}_w - \mathbf{p}_w^{init}) \in \mathbb{R}^3$  is the wrist-position deflection from the initial one,  $k_g$  is a gradient gain.

The structure of the control command is as follows. The first term is the end-effector orientation control projected onto the null-space of the coupling inertia matrix: this term can accomplish the end-effector orientation control under the reactionless constraint. The second term minimizes the following potential function to stabilize the wrist position:

$$V = \frac{1}{2} \|\Delta \mathbf{p}_w\|^2. \quad (8)$$

This term does not disturb the higher priority tasks because it is projected onto the null-space of all higher priority tasks.

Here, it must be noted that  $\bar{\mathbf{J}}_{\omega}^+$  includes the algorithmic singularities, which occur when the end-effector control and the reactionless constraint are conflict. The details of this singularity will be described, below.

#### 4.2.3. Numerical simulation

In what follows, we examine the performance under (7) by comparing to the following conventional inverse Jacobian controller with motionless of the positioning subchain. We assume two situations: (i) observation of a satellite to be serviced (Fig. 6 (a)) and (ii) inspection for own satellite mounted devices (Fig. 6 (b)).

First, we verify the satellite observation case. The initial configuration is set as  $\boldsymbol{\theta}(0) = [-90 \ -30 \ 0 \ -70 \ 180 \ -30 \ 0]^T$  deg as shown in Fig. 6 (a), the reference angular velocity is  $\boldsymbol{\omega}_e^{ref} = \pi[s(t) \ 0 \ 0]^T$ , where  $0 \leq s(t) \leq 1$  denotes a fifth-order polynomial interpolation. The simulation was conducted with the simulation time 20 s. The simulation results are displayed in Fig. 7.

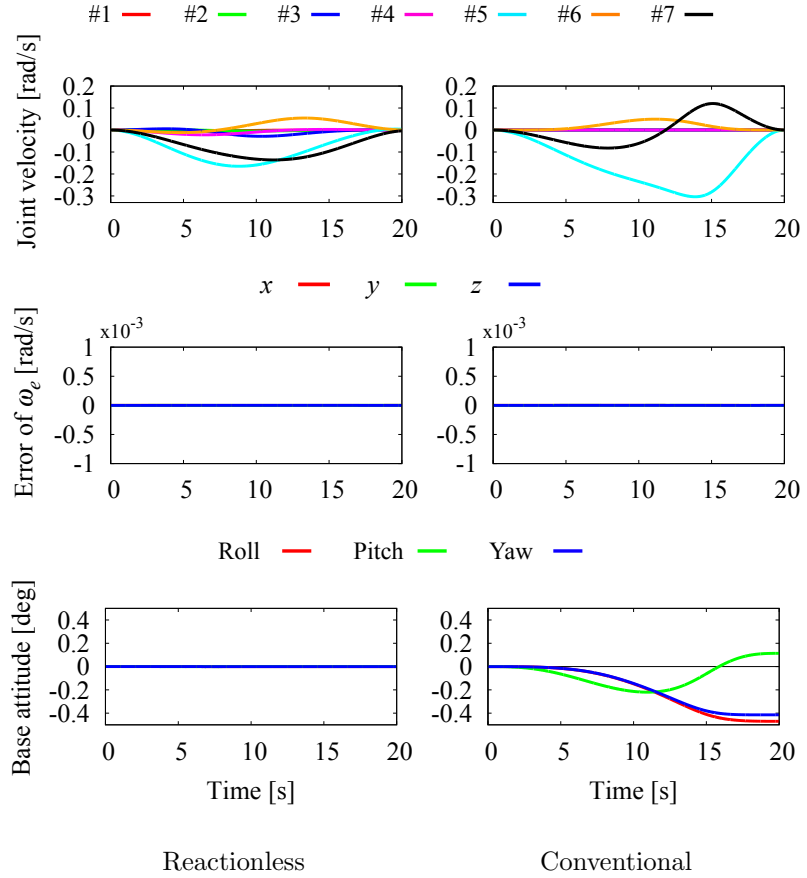


Figure 7: Simulation result under the satellite observation mission (Fig. 6 (a)). The result shows that reactionless task can be accomplished, while a large base attitude deviation is observed under the conventional control method.

These are obtained with  $k_g = 100$ . In both methods, it can be seen that the end-effector task is accomplished. It is also seen that the base attitude deviation is not observed under reactionless motion control. The reactionless manner can be realized with the relatively small motion of the positioning subchain, see the figure of joint velocity. We should note that a relatively large base attitude deviation <sup>1</sup> is induced under the conventional control method, despite the low inertia parameters of the wrist.

In the second case, we assume that the initial configuration is set to

---

<sup>1</sup>The limitation of the base attitude deviation is 0.05 deg in the ETS-VII missions.

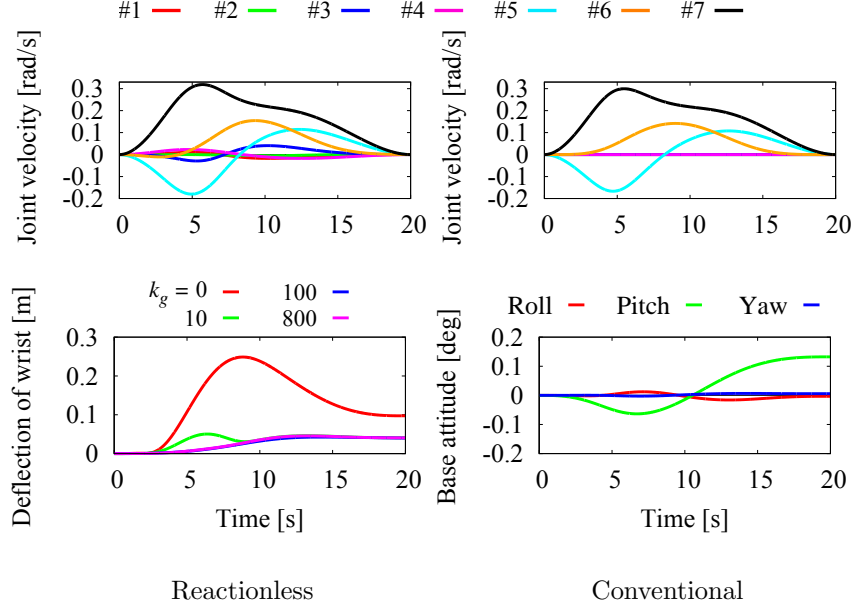


Figure 8: Simulation result under the inspection of own-satellite mounted devices (Fig. 6 (b)).

$[90 \ -20 \ 180 \ 110 \ 0 \ 20 \ 0]^T$  deg as shown in Fig. 6 (b), the desired end-effector velocity is  $\omega_e^{ref} = \pi[0 \ 0 \ -s(t)]^T$  rad/s. The other conditions are same as the previous ones. The simulation result is displayed in Fig. 8. First, it becomes apparent that the effect of the cost function leads to a sufficiently small deviation from the initial wrist position as shown in Fig. 8. In the case of the conventional controller, the relatively large base attitude deviation is also confirmed.

In summary, in the inspection task, even with the small mass and inertia moment of the wrist subchain, a large base attitude deviations were observed. From the results, we can conclude that this reactionless motion task is a useful way to overcome this problem.

## 5. The singularities within the reactionless inspection task

### 5.1. Problem statement

In this section, we deal with the singularities within the proposed reactionless task. Within the reactionless camera inspection, there are three type of singularities, as follows:

- Kinematic singularity:  $\det(\mathbf{J}_\omega \mathbf{J}_\omega^T) = 0$
- Singularities of the coupling inertia matrix:  $\det(\tilde{\mathbf{M}}_{\omega m} \tilde{\mathbf{M}}_{\omega m}^T) = 0$
- Algorithmic singularities:  $\det(\bar{\mathbf{J}}_\omega \bar{\mathbf{J}}_\omega^T) = 0$  with non-singular  $\mathbf{J}_\omega$  and full row-rank  $\tilde{\mathbf{M}}_{\omega m}$

Among them, kinematic singularities have been much discussed by various researchers, e.g. [32, 33]. From these results, the kinematic singularity can be dealt with some singularity treatment techniques. The most famous one is the damped least-squares inverse (DLS) [34]. Using these method, growth up of the joint velocity can be suppressed through adding a damping factor. A drawback of this method is causing an error on the task space, both speed and direction. On the other hand, we have proposed another method, which is called the Singularity Consistent method [35]. Under this method, the manipulator can follow the desired path without causing a large joint velocity<sup>2</sup>. In both method, the feasibility has been verified under the kinematic singularities. Hence, we will not pay attention this type of singularity below.

On the other hand, the second and third one have not been treated. However, the singularities of the coupling inertia matrix is not a problem, because we use the null-space of the coupling inertia matrix. In (7), the rank of  $\bar{\mathbf{J}}_\omega$  depends on the condition of  $\mathbf{J}_\omega$  only, since the rank of  $\mathbf{P}_{RNS}$  cannot be lower than 3 with any configurations: e.g. at the singular configuration the rank increases more than 4. Hence, we will not also pay attention this type of singularities.

On the other hand, the algorithmic singularities must be taken into account. The inversion of  $\bar{\mathbf{J}}_\omega$  can be rewritten through SVD in the following form:

$$\bar{\mathbf{J}}_\omega^+ = \frac{1}{\sigma_1} \mathbf{v}_1 \mathbf{u}_1^T + \frac{1}{\sigma_2} \mathbf{v}_2 \mathbf{u}_2^T + \frac{1}{\sigma_3} \mathbf{v}_3 \mathbf{u}_3^T \quad (9)$$

where,  $\sigma_1 \geq \sigma_2 \geq \sigma_3$  are the singular values,  $\mathbf{v}_i \in \mathbb{R}^7$ ,  $\mathbf{u}_i \in \mathbb{R}^3$  are the left and right singular vectors associated with  $\sigma_i$ . Near the singularities, the last term of (9) takes a large value due to small value of  $\sigma_3$ .

In what follows, we show an example of the algorithmic singularity. We assume the inspection task with the same initial configuration which was used

---

<sup>2</sup>The term “Path” is distinguished from “Trajectory”: the former one means geometrical path and the later one includes time-parameter.

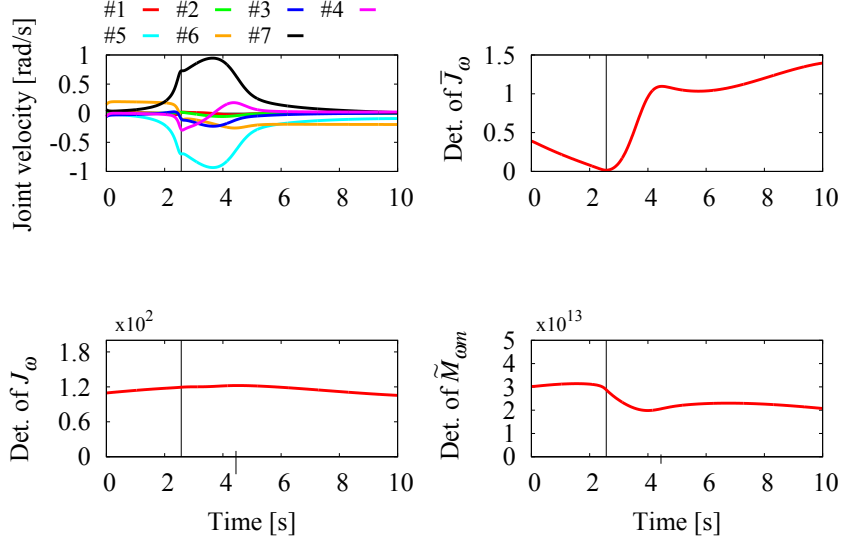


Figure 9: An example of the algorithmic singularity within the proposed method.

in the satellite observation task as shown in Fig. 6 (a). On the other hand, the desired angular velocity is commanded as  $\boldsymbol{\omega}_e^{ref} = [0 \ -0.2 \ 0]^T$  rad/s. The simulation results are displayed in Fig. 9. In the graphs, the solid line in black represents the time when the manipulator is passing through near the singularity ( $t \approx 2.57$ ). At that time, the determinant of  $\bar{J}_\omega$  takes a small value without causing  $\det(\mathbf{J}_\omega \mathbf{J}_\omega^T) = 0$  and  $\det(\tilde{\mathbf{M}}_{\omega m} \tilde{\mathbf{M}}_{\omega m}^T) = 0$  as shown in Fig. 9. Hence, this singularity can be recognized as the algorithmic one. Within the near singularity, we observe that joint 5 and 7 rotate around opposite direction with large joint velocity. This kind of behavior has been observed at the singularity of Euler angle [36] and the kinematic singularity of wrist assemblies.

From the empirically obtained results, this algorithmic type of singularity does not seem to happen frequently. Besides, even if the singularity happens, we will show a well-known singularity treatment technique, so-called the damped least-squares inverse, can relieve the influence of the singularity.

### 5.2. The damped least-squares inverse based singularity treatment

The damped least-squares inverse is a well-known approach for singularity problem. This method is adding a damping factor into the denominators in (9) to avoid causing a large joint velocity. Among various types of the

damped least-squares inverse, we use that with numerical filtering because this method does not cause a large error. By using this method, the inverse matrix of  $\bar{\mathbf{J}}_\omega$  is obtained in the following form:

$$\bar{\mathbf{J}}_\omega^\# = \bar{\mathbf{J}}_\omega^T \left( \bar{\mathbf{J}}_\omega \bar{\mathbf{J}}_\omega^T + \lambda^2 \mathbf{u}_3 \mathbf{u}_3^T \right)^{-1} \quad (10)$$

where,  $\lambda$  is a damping factor,  $\mathbf{u}_3 \in \mathbb{R}^3$  is the left singular vector associated with the minimum singular value  $\sigma_3$ ,  $(\circ)^\#$  represents the damped least-squares inverse. By replacing the pseudoinverse solution with the damped least one, we can deal with the singularity problem.

Through Singular Value Decomposition, (10) can be rewritten as:

$$\bar{\mathbf{J}}_\omega^\# = \sum_{i=1}^2 \frac{1}{\sigma_i} \mathbf{v}_i \mathbf{u}_i^T + \frac{\sigma_3}{\sigma_3^2 + \lambda^2} \mathbf{v}_3 \mathbf{u}_3^T \quad (11)$$

where,  $\sigma_1 \geq \sigma_2 \geq \sigma_3$  are the singular value of  $\bar{\mathbf{J}}_\omega$  and  $\mathbf{u}_i \in \mathbb{R}^3$ ,  $\mathbf{v}_i \in \mathbb{R}^7$  is the left and right singular vector associated with  $\sigma_i$ . Compared with (9), it can be seen that the damped least square inverse with numerical filtering is inserting the damping factor into only the last term which is related to the minimum singular value. Hence, compared to the basic damped least square inverse, which adds a damping into all terms, the error of the solution can be reduced [37].

Based on [34], the damping factor is obtained as follows:

$$\lambda^2 = \begin{cases} 0 & \varepsilon < \sigma_3 \\ (1 - \frac{2\sigma_3^2}{\varepsilon^2} + \frac{\sigma_3^4}{\varepsilon^4})\lambda_{max}^2 & \sigma_3 \leq \varepsilon \end{cases} \quad (12)$$

where,  $\varepsilon$  defines the singular region, which is conveniently introduced in the neighborhood of the singularity,  $\lambda_{max}$  sets the maximum value of the damping factor. Note that we added an additional term, the  $\sigma_3^4$  related term, into (12) to obtain a smooth transition on the border of the singular region, because the original one did not consider the continuity at the first differential in terms of  $\sigma_3$ .

The performance of the damped least-squares inverse for this controller is verified via numerical simulation. The simulation conditions are the same as in Section 5.1. The singular region is defined as  $\varepsilon = 0.2$  and the maximum damping value set to  $\lambda_{max}^2 = 2$ .

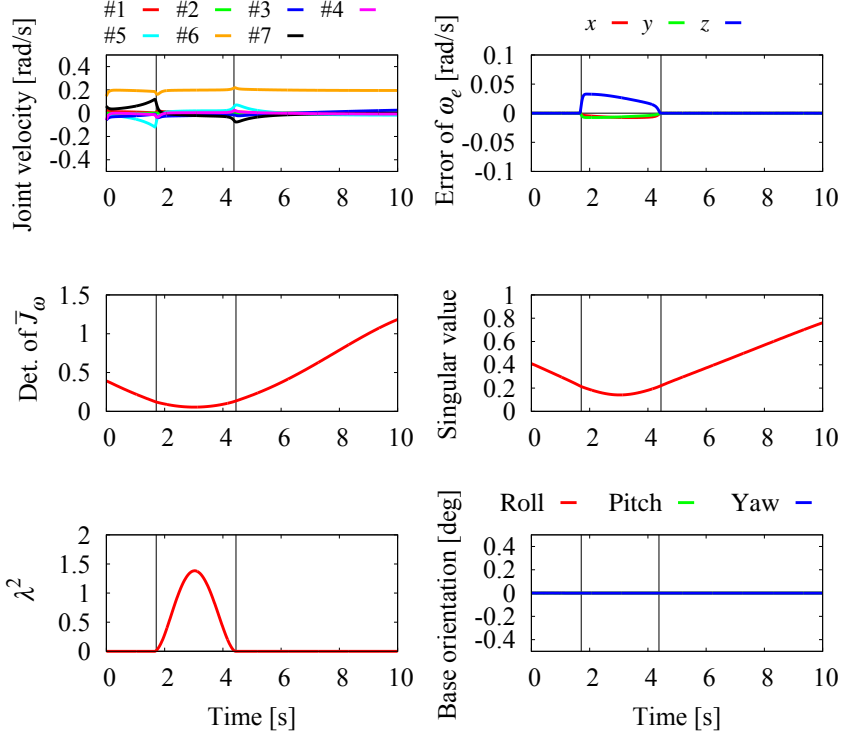


Figure 10: These figures show that the inspection task can be accomplished without causing a large joint velocity within the singular region.

The results are displayed in Fig. 10. In the graphs, the singular region is indicated as the time duration between the two black lines ( $1.71 \leq t \leq 4.18$ ). From the results, the growth up of the joint velocity can be avoided through the damping factor. However, the end-effector tracking error can be observed within the singular region. This is caused by adding the damping factor into the last term in (11). On the other hand, the base attitude deviation is not induced even if within the singular region.

At the inspection task, high accuracy of the end-effector orientation control would not be required, because camera view can be corrected through revising the image. Hence, we can conclude that this motion task would be useful in the presence of the singularity.

## 6. Energy consumption analysis under zero base-attitude deviation

Under the inspection task, despite the reaction wheels can compensate the base disturbance induced by the manipulator motions because that is not so large especially as shown in Fig. 8, we will show that the reaction wheels have a disadvantage in terms of energy consumption.

First, we identify the minimum energy motion under zero base-attitude deviation ( $\boldsymbol{\omega}_b \approx \mathbf{0}$ ) and show that it is almost equivalent to reactionless motion control. This character arises from, under reactionless motion control, the no usage of reaction wheels and its high amount of energy consumption. Note that we restrict our attention to the system which consists of one manipulator and three reaction wheels, for the sake of simplicity.

### 6.1. Kinetic energy representation in terms of the joint velocity

In this work, we assume that kinetic energy is used to evaluate energy consumption. For the sake of simplicity, we ignore energy losses arising from friction, heat and electric part. The kinetic energy of the space robot system can be written as [3, 20]:

$$T = \frac{1}{2} \boldsymbol{\omega}_b^T \tilde{\mathbf{M}}_\omega \boldsymbol{\omega}_b + \boldsymbol{\omega}_b^T [\tilde{\mathbf{M}}_{\omega_m} \quad \tilde{\mathbf{M}}_{\omega_r}] \begin{bmatrix} \dot{\boldsymbol{\theta}} \\ \dot{\boldsymbol{\phi}} \end{bmatrix} + \frac{1}{2} [\dot{\boldsymbol{\theta}}^T \quad \dot{\boldsymbol{\phi}}^T] \begin{bmatrix} \tilde{\mathbf{M}}_m & \mathbf{0} \\ \mathbf{0} & \tilde{\mathbf{M}}_r \end{bmatrix} \begin{bmatrix} \dot{\boldsymbol{\theta}} \\ \dot{\boldsymbol{\phi}} \end{bmatrix} \quad (13)$$

where, the first term on the r.h.s. represents the partial kinetic energy stemming from base rotation, the second term is coupling kinetic energy between the base and the manipulator or the reaction wheels. Finally, the third term is the partial kinetic energy produced by the manipulator and the reaction wheels.

With the assumption  $\boldsymbol{\omega}_b \approx \mathbf{0}$ , (13) can be simplified as:

$$T = \frac{1}{2} \dot{\boldsymbol{\theta}}^T \tilde{\mathbf{M}}_m \dot{\boldsymbol{\theta}} + \frac{1}{2} \dot{\boldsymbol{\phi}}^T \tilde{\mathbf{M}}_r \dot{\boldsymbol{\phi}} \quad (14)$$

In addition, from angular momentum conservation, the reaction wheel speed can be represented as a function of the joint velocity,  $\dot{\boldsymbol{\phi}} = -\tilde{\mathbf{M}}_{\omega_r}^{-1} \tilde{\mathbf{M}}_{\omega_m} \dot{\boldsymbol{\theta}}$ . By substituting the above equation into (14), we can obtain the kinetic energy

as a function of the joint velocity as follows:

$$\begin{aligned}
T &= \frac{1}{2} \dot{\theta}^T \left( \tilde{\mathbf{M}}_m + \tilde{\mathbf{M}}_{\omega m}^T (\tilde{\mathbf{M}}_{\omega r} \tilde{\mathbf{M}}_r^{-1} \tilde{\mathbf{M}}_{\omega r}^T)^{-1} \tilde{\mathbf{M}}_{\omega m} \right) \dot{\theta} \\
&= \frac{1}{2} \dot{\theta}^T \left( \tilde{\mathbf{M}}_m + I_r^{-1} \tilde{\mathbf{M}}_{\omega m}^T \tilde{\mathbf{M}}_{\omega m} \right) \dot{\theta} \\
&= \frac{1}{2} \dot{\theta}^T \hat{\mathbf{M}} \dot{\theta}
\end{aligned} \tag{15}$$

where,  $\hat{\mathbf{M}} = \hat{\mathbf{M}}_m + \hat{\mathbf{M}}_r$  is the inertia matrix of the manipulator under zero attitude deviation,  $\hat{\mathbf{M}}_m = \tilde{\mathbf{M}}_m$ ,  $\hat{\mathbf{M}}_r = I_r^{-1} \tilde{\mathbf{M}}_{\omega m}^T \tilde{\mathbf{M}}_{\omega m} \in \mathbb{R}^{n \times n}$  are that associated with the manipulator and the reaction wheels, respectively. In the above derivation, we assume that  $\tilde{\mathbf{M}}_{\omega r} \approx \tilde{\mathbf{M}}_r$  and  $\tilde{\mathbf{M}}_r = \text{diag}(I_r, I_r, I_r)$ . Besides, we assume that the reaction wheels are arranged on each orthogonal axis on the base coordinate according to zero-momentum stabilization, and these inertia moments are same.

### 6.2. Instantaneous minimum energy motion under zero base-attitude deviation

Equation (15) represents kinetic energy under zero base-attitude deviation. With using the same way as the coupling map [38], the instantaneous minimum energy motion can be obtained through SVD of the inertia matrix  $\hat{\mathbf{M}} = \hat{\mathbf{M}}_m + \hat{\mathbf{M}}_r$ :

$$\hat{\mathbf{M}} = \sigma_1 \mathbf{u}_1 \mathbf{v}_1^T + \sigma_2 \mathbf{u}_2 \mathbf{v}_2^T + \cdots + \sigma_n \mathbf{u}_n \mathbf{v}_n^T \tag{16}$$

where,  $\sigma_i$  ( $\sigma_1 \geq \sigma_2 \geq \cdots \geq \sigma_n$ ) is singular value,  $\mathbf{u}_i$  and  $\mathbf{v}_i$  are the left and right singular vectors. In this equation, physically,  $\mathbf{v}_i$  stands for the normalized joint velocity and  $\sigma_i$  represents kinetic energy induced by the joint motion  $\mathbf{v}_i$ . Because  $\sigma_n$  represents the instantaneous minimum kinetic energy,  $\mathbf{v}_n^T$  represents the instantaneous minimum energy motion.

### 6.3. Equivalence between reactionless motion and instantaneous minimum energy motion, through numerical analysis

Here, we compare reactionless motion and the instantaneous minimum energy motion via numerical analysis. For the sake of simplicity, we focus on only models which has one-DoF reactionless motion.

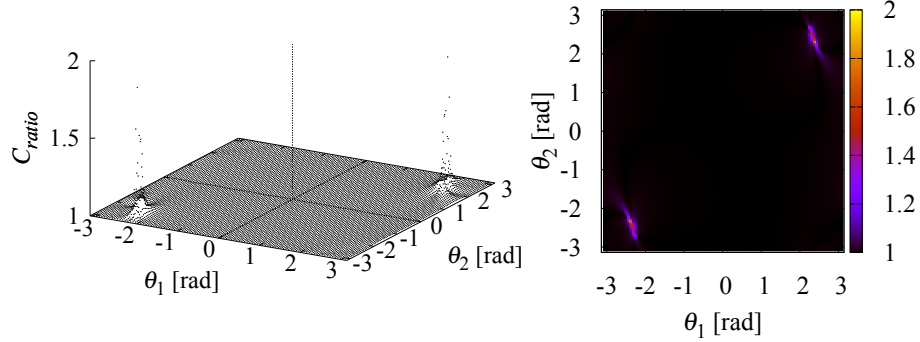


Figure 11: The distribution of the cost function with the two-DoF model.

### 6.3.1. Two-DoF planar manipulator

First, a two-DoF planar model is considered, which is shown in Fig. 1. The link lengths, masses and inertia moments are set to  $l_i = 1.0$  m,  $m_i = 100$  kg and  $I_i = 8.3$  kgm<sup>2</sup> ( $i = 1, 2$ ), respectively. The reaction wheel's mass and inertia moment are set to  $m_r = 10$  kg,  $I_r = 0.11$  kgm<sup>2</sup>. The manipulator attachment position is defined as  $r = 0.945$  m,  $\psi = 0$  rad, whose meaning of parameters are same as Fig. 1.

Here, we consider the following cost function to evaluate the equivalence between reactionless motion and the instantaneous minimum energy motion:

$$C_{ratio} = \frac{T_{RNS}}{T_{min}} \quad (17)$$

where,  $T_{RNS}$ ,  $T_{min}$  are the kinetic energy under reactionless motion control and the instantaneous minimum one. Because  $T_{RNS} \geq T_{min}$  at all configurations,  $C_{ratio} \geq 1$  is ensured.  $C_{ratio}$  takes close to 1 means these motion are equivalent. This function will be calculated at 10000 points in the joint space with  $-\pi \leq \theta_i \leq \pi$ , ( $i = 1, 2$ ). For each coordinate, joint angle are discretized with  $\Delta\theta_i = 6.28 \times 10^{-2}$  rad.

According to (16),  $\dot{\theta}_{min}$  can be obtained as  $\mathbf{v}_2$  and reactionless motion is obtained through SVD of the coupling inertia matrix. The distribution of  $C_{ratio}$  is displayed in Fig. 11. From the result, we can confirm that  $C_{ratio} \approx 1$  at almost all points. Indeed, the average of  $C_{ratio}$  is 1.002 among all points. Hence, these motions are equivalent in this model. Here, we should note that there are large errors in specific points. This non-correspondence will be discussed below.

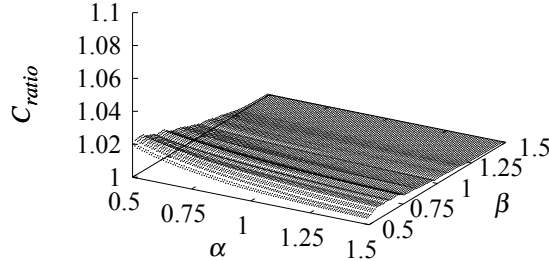


Figure 12: This figure shows how the average of  $C_{ratio}$  is affected by parameter variation.

### 6.3.2. Influence arising from parameters variation

Before discussing spatial model, we should identify the influence arising from parameter variation. Here, we focus on total link mass and the CoM position of each link according to the following equation:

$$m_i^* = \alpha m_i \quad (18)$$

$$l_{ci}^* = \beta l_{ci} \quad (19)$$

where,  $0.5 \leq \alpha \leq 1.5$ ,  $0.5 \leq \beta \leq 1.5$  are scaling factors,  $m_i$ ,  $l_{ci} = l_i/2$  are the original mass and length to the CoM position of each link as explained above ( $m_i = 100$  kg,  $l_i = 1$  m).  $(\circ)^*$  denotes the modified parameter. Average of  $C_{ratio}$  under the parameter variation is displayed in Fig. 12. This figure shows that reactionless motion coincides with instantaneous minimum motion even if parameters are changed. In particular, high equivalence can be observed when  $\alpha$  takes large values.

### 6.3.3. Four-DoF spatial manipulator

Here, we identify the equivalence with a four-DoF spatial manipulator. As the our manipulator model, the positioning subchain of the seven-DoF redundant manipulator is considered. The reaction wheel parameters are same as one which was used in the planar case. In this case, the same cost function is also used to evaluate the equivalence. The calculation range is as

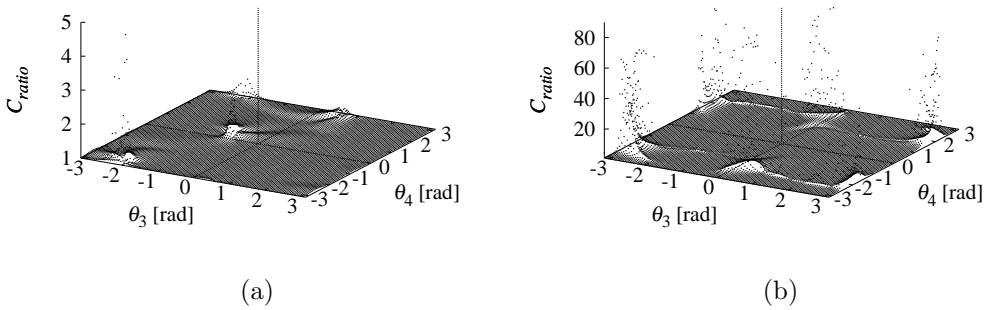


Figure 13: The disistribution of cost function with the four-DoF spatial manipulator model:  
(a) regularly appearing distribution  $(\theta_1, \theta_2) = (-3.05, 0.403)$  rad and (b) near the singularity  $(\theta_1, \theta_2) = (-\pi, 0)$  rad.

follows:

$$\begin{aligned} -\pi &\leq \theta_i \leq \pi \\ \Delta\theta_i &= 0.125 \text{ rad } (i = 1, 3, 4) \end{aligned} \quad (20)$$

$$\begin{aligned} -\frac{\pi}{2} &\leq \theta_2 \leq \frac{\pi}{2} \\ \Delta\theta_2 &= 0.0628 \text{ rad} \end{aligned} \quad (21)$$

where, we restrict the range of joint 2 because almost all configurations over the above range have no meaning due to the collision with the satellite. Totally, the cost function is calculated at  $6.25 \times 10^6$  points.

Because of too many parameters to draw graph, we show the distribution of  $C_{ratio}$  parametrized for joint 1 and 2. First, we show a distribution map which does not include large errors in Fig. 13 (a). The map was obtained with parametrized for  $(\theta_1, \theta_2) = (-3.05, 0.403)$  rad. Except few configurations, reactionless motion coincides the energy minimum motion as seen in the planar case. However, we observe inconsistency with specific configurations. An example is shown in Fig. 13 (b) with parametrized for  $(\theta_1, \theta_2) = (-\pi, 0)$  rad. Despite these large errors, the average value of  $C_{ratio}$  is 1.14. Hence, reactionless motion produces almost minimum energy. In what follows, we discuss the reason of the equivalence and the inconsistency.

### 6.3.4. Discussion about the equivalence

Here, we discuss why these motions are equivalent. To answer the question, we should identify a property of kinetic energy produced by both manipulator and reaction wheels under zero base-attitude deviation. This property appears in the inertia matrix.  $\hat{\mathbf{M}}_m$  and  $\hat{\mathbf{M}}_r$  are rewritten in the following form:

$$\hat{\mathbf{M}}_m = \sum_{i=1}^n \left\{ m_i \mathbf{J}_{vi}^T \mathbf{J}_{vi} + \mathbf{J}_{\omega i}^T \mathbf{I}_i \mathbf{J}_{\omega i} \right\} \quad (22)$$

$$\begin{aligned} \hat{\mathbf{M}}_r = & \frac{1}{I_r} \sum_{i=1}^n \left\{ m_i^2 \mathbf{J}_{vi}^T \mathbf{r}_i^{\times T} \mathbf{r}_i^{\times} \mathbf{J}_{vi} + \mathbf{J}_{\omega i}^T \mathbf{I}_i \mathbf{I}_i \mathbf{J}_{\omega i} + \right. \\ & \left. m_i \mathbf{J}_{\omega i}^T \mathbf{I}_i \mathbf{r}_i^{\times} \mathbf{J}_{vi} + [m_i \mathbf{J}_{\omega i}^T \mathbf{I}_i \mathbf{r}_i^{\times} \mathbf{J}_{vi}]^T \right\} \end{aligned} \quad (23)$$

where,  $m_i$ ,  $\mathbf{I}_i \in \mathbb{R}^3$  are  $i$ th link mass and inertia tensor,  $\mathbf{J}_{vi}$ ,  $\mathbf{J}_{\omega i} \in \mathbb{R}^{3 \times n}$  stand for the Jacobian w.r.t. linear and angular velocity of each link,  $\mathbf{r}_i \in \mathbb{R}^3$  is the position vector of  $i$ th link CoM w.r.t. the base CoM. Here, we assume general  $n$ -link manipulator model. Note that base linear motion related terms are ignored for the sake of simplicity.

From (22), it can be seen that the kinetic energy induced by the manipulator motion is represented as a linear function in terms of the inertia parameters of manipulator. On the other hand, reaction wheel related energy is a quadratic function in terms of same parameters; it is also proportion to the inverse of the inertia moment of the reaction wheel, which is usually enough smaller than 1. Hence, we can conclude that the reaction wheel producing kinetic energy is far larger than the manipulator's one. This feature would make reactionless motion potentially effective in terms of energy consumption because no usage of reaction wheels.

On the other hand, compared with the results in Fig. 2 (b) and Fig. 11, we can find that the inconsistency happens around the singularity of the coupling inertia matrix. In particular, at the singular configuration, any motion does not disturb the base attitude because the null-space of the coupling inertia matrix coincides with the tangential space of joint space  $T_\theta(\mathbb{R}^2)$ : namely an additional reactionless motion vector appears at the singularity. In this case, reactionless motion must be energy minimum. On the other hand, near the singularities, reactionless motion does not coincide with the instantaneous energy minimum motion, in general. Since the base disturbance is quite

small near the singularity: e.g. reaction wheel is hardly needed, reactionless motion can be different from the minimum energy one.

#### 6.4. Comparison study under the inspection task

##### 6.4.1. Simulation condition

Finally, we evaluate the performance of using reactionless motion control in terms of energy consumption at the inspection maneuver. From the above analysis, reactionless motion is nearly energy minimum and reaction wheels are needed a large energy to compensate a base disturbance.

We consider the following cost functions to evaluate the performance:

$$C_{max} = \frac{1}{2} \max_{t_0 \leq t \leq t_f} (\dot{\theta}^T(t) \hat{M} \dot{\theta}(t)) \quad (24)$$

$$C_{sum} = \frac{1}{2} \int_{t_0}^{t_f} \dot{\theta}^T(t) \hat{M} \dot{\theta}(t) dt \quad (25)$$

In order to realize zero base-attitude deviation with reaction wheels, the reaction wheel torque must ensure the following condition:

$$\tau_r^{ref} = -\frac{d}{dt}(\tilde{M}_{wm} \dot{\theta}^{ref}(t)) \quad (26)$$

where,  $\dot{\theta}^{ref}$  is the pre-defined reference control command for the manipulator.

We compare the above costs under the camera inspection task under five conditions with some initial configurations and the desired motions. At all of them, simulation time is set as 20 s and the comparison controller is the inverse Jacobian controller using only the wrist assembly as explained in the previous section.

##### 6.4.2. Simulation results

First, we show an example. The conditions were same as ones which were considered in Section 4 (the case of Fig. 6 (a)). The results are displayed in Fig. 14. We can see that the kinetic energy produced by the reaction wheel is quite larger than that by the manipulator motion. As a result, reactionless motion control has an advantage in terms of energy consumption as described above. In addition, if we plan to perform this inspection task with reaction wheels, the manipulator has to be driven at lower speed because the limitation of the reaction wheel torque general poor: the limitation is 0.1 Nm in the ETS-VII.

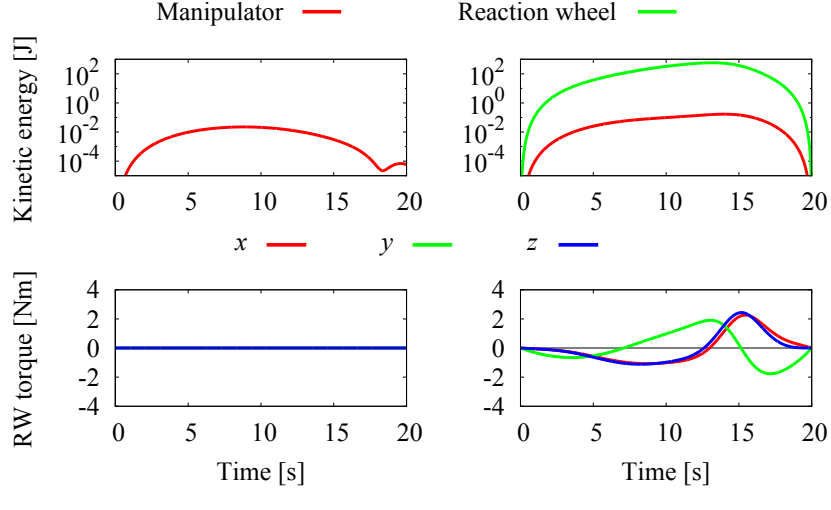


Figure 14: An example of energy consumption comparison.

Next we compare the cost over five conditions. The results are displayed with bar graph in Fig. 15. The red bar expresses the result under reactionless motion control; the green bar is that with the reaction wheels. Note that the axis of kinetic energy is represented as log scale. From the results, it can be seen that energy consumption under reactionless motion is also quite smaller than that of the reaction wheel based method. Actually, almost  $10^3$  times reduction is observed in the both cost functions. This result is due to the large energy consumption of reaction wheel as explained in (23). In summary, we can conclude that energy consumption can be largely reduced in addition to mission duration, by using reactionless motion control.

## 7. Conclusion

In this work, we tackled the following three issues in reactionless motion control. (i) motion analysis of reactionless motion control (ii) proposal of a motion task suitable for execution under reactionless motion control and (iii) energy consumption under zero base-attitude deviation.

Despite some researchers have addressed reactionless motion control, reactionless motion itself seems to be unclear. We analyzed reactionless motion with a planar two-DoF model through numerical calculation. From the result, we show a new character of reactionless motion. Among its

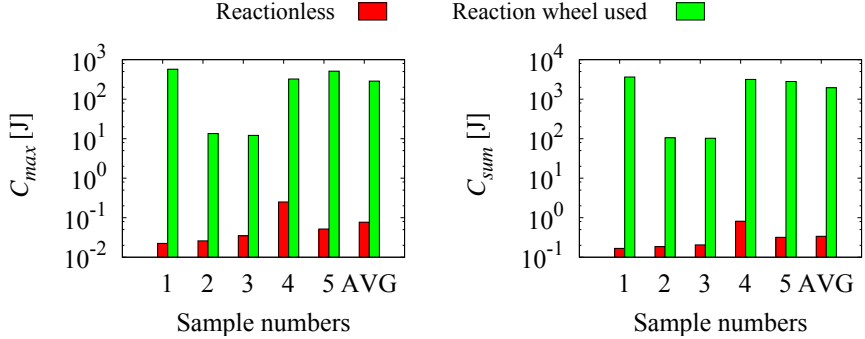


Figure 15: Comparison of energy consumption under five conditions

model parameters, the manipulator attachment position plays an important role as a bifurcation parameter. When a displacement between the base Com and the manipulator attachment position is large, occurrence of fixed points/singularities was observed. If we plan to use reactionless motion control, this character should be included in design phase. The manipulator design for reactionless motion will be considered as the future task.

On the other hand, as a practical use of reactionless motion, we proposed an inspection task using a hand camera with a seven-DoF redundant manipulator. With this model, its reactionless motion is approximately represented a superposition between predominant wrist and elbow motion. Based on the predominant wrist motion, we designed a controller for inspection task based on the theory of task priority. The base attitude (reactionless) constraint was considered as the primary task; the end-effector orientation control is the second one; the wrist position stabilization was performed as the third priority. From the verification via numerical simulations, we showed this reactionless task can be useful compared with the traditional inverse Jacobian controller. In addition, we showed the effectiveness of the damped least-squares inverse to the algorithmic singularity within the end-effector reactionless control.

Finally, we discussed energy consumption under zero base-attitude deviation. We evaluated the performance of energy consumption with kinetic energy produced by both the manipulator and reaction wheels. Mathematically, the kinetic energy of reaction wheel is represented as a quadratic function of the parameters of the manipulator, while the kinetic energy of the manipulator is a linear function of the parameters. This feature makes reactionless motion effectiveness in terms of energy consumption. Indeed, reactionless motion produces almost minimum energy. Under the inspection maneuver,

we verified the energy consumption of reactionless motion compared with a reaction wheel based reaction compensation. As a result,  $10^3$  times reduction of energy consumption can be observed using reactionless motion.

- [1] A. Flores-Abad, O. Ma, K. Pham, S. Ulrich, A review of space robotics technologies for on-orbit servicing, *Progress in Aerospace Sciences* 68 (2014) 1–26.
- [2] Z. Vafa, S. Dubowsky, On the dynamics of manipulators in space using the virtual manipulator approach, in: *Proceedings of IEEE International Conference on Robotics and Automation*, 1987, pp. 579–585.
- [3] Y. Masutani, F. Miyazaki, S. Arimoto, Sensory feedback control for space manipulators, in: *Proceedings of IEEE International Conference on Robotics and Automation*, 1989, pp. 1346–1351.
- [4] Y. Umetani, K. Yoshida, Resolved motion rate control of space manipulators with generalized Jacobian matrix, *IEEE Transactions on Robotics and Automation* 5 (3) (1989) 303–314.
- [5] S. Moosavian, E. Papadopoulos, Modified transpose Jacobian control of robotic systems, *Automatica* 43 (7) (2007) 1226–1233.
- [6] K. Yoshida, N. Sashida, R. Kurazume, Y. Umetani, Modeling of collision dynamics for space free-floating links with extended generalized inertia tensor, in: *Proceedings of IEEE International Conference on Robotics and Automation*, 1992, pp. 899–904.
- [7] Y. Umetani, K. Yoshida, Workspace and Manipulability Analysis of Space Manipulator, *Transactions of the Society of Instrument and Control Engineers* 8 (1) (2001) 1–8.
- [8] K. Yoshida, Practical coordination control between satellite attitude and manipulator reaction dynamics based on computed momentum concept, in: *Proceedings of IEEE/RSJ International Conference on Intelligent Robots and Systems*, 1994, pp. 1578–1585.
- [9] F. Aghili, Coordination control of a free-flying manipulator and its base attitude to capture and detumble a noncooperative satellite, in: *Proceedings of IEEE/RSJ International Conference on Intelligent Robots and Systems*, 2009, pp. 2365–2372.

- [10] K. Yoshida, Engineering test satellite VII flight experiments for space robot dynamics and control: theories on laboratory test beds ten tears ago, now in orbit, *The International Journal of Robotics Research* 22 (5) (2003) 321–335.
- [11] S. Dubowsky, M. Torres, Path planning for space manipulators to minimize spacecraft attitude disturbances, in: *Proceedings of IEEE International Conference on Robotics and Automation*, 1991, pp. 2522–2528.
- [12] S. Dubowsky, E. Papadopoulos, The kinematics, dynamics, and control of free-flying and free-floating space robotic systems, *IEEE Transactions on Robotics and Automation* 9 (5) (1993) 531–543.
- [13] D. Nenchev, Y. Umetani, K. Yoshida, Analysis of a redundant free-flying spacecraft/manipulator system, *IEEE Transactions on Robotics and Automation* 8 (1) (1992) 1–6.
- [14] D. Nenchev, K. Yoshida, P. Vichitkulsawat, M. Uchiyama, Reaction null-space control of flexible structure mounted manipulator systems, *IEEE Transactions on Robotics and Automation* 15 (6) (1999) 1011–1023.
- [15] K. Yoshida, K. Hashizume, S. Abiko, Zero reaction maneuver: flight validation with ETS-VII space robot and extension to kinematically redundant arm, in: *Proceedings of IEEE International Conference on Robotics and Automation*, 2001, pp. 441–446.
- [16] K. Yoshida, K. Hashizume, D. Nenchev, N. Inaba, M. Oda, Control of a space manipulator for autonomous target capture - ETS-VII flight experiments and analysis, in: *Proceedings of AIAA Guidance, Navigation, and Control Conference and Exhibit*, 2000, pp. 2000–4376.
- [17] D. Hirano, Y. Fujii, S. Abiko, R. Lamariello, K. Nagaoka, K. Yoshida, Simultaneous Control for End-Point Motion and Vibration Suppression of a Space Robot Based on Simple Dynamic Model, in: *Proceedings of IEEE International Conference on Robotics and Automation*, 2014, pp. 6631–6637.
- [18] T. Oki, H. Nakanishi, K. Yoshida, Whole-body motion control for capturing a tumbling target by a free-floating space robot, in: *Proceedings*

of IEEE/RSJ International Conference on Intelligent Robots and Systems, IEEE, 2007, pp. 2256–2261.

- [19] D. Nenchev, K. Yoshida, Y. Umetani, Analysis, design and control of free-flying space robots using fixed-attitude-restricted jacobian matrix, in: Proceedings of The Fifth International Symposium on Robotics Research, 1990, pp. 251–258.
- [20] D. Dimitrov, K. Yoshida, Utilization of the bias momentum approach for capturing a tumbling satellite, in: Proceedings of IEEE/RSJ International Conference on Intelligent Robots and Systems, 2004, pp. 3333–3338.
- [21] S. V. Shah, I. Sharf, A. Misra, Reactionless path planning strategies for capture of tumbling objects in space using a dual-arm robotic system, in: Proceedings of AIAA Guidance, Navigation, and Control Conference, Reston, Virginia, 2013.
- [22] A. Pisculli, L. Felicetti, P. Gasbarri, G. Palmerini, M. Sabatini, A reaction-null/Jacobian transpose control strategy with gravity gradient compensation for on-orbit space manipulators, Aerospace Science and Technology 38 (2014) 30–40.
- [23] D. N. Nenchev, K. Yoshida, Singularity-consistent teleoperation techniques for redundant free-flying robots, in: Proceedings of AIAA Guidance, Navigation, and Control Conference, 1999, pp. 1895–1902.
- [24] Y. Nakamura, S. Ito, Lowering energy consumption of Space robot systems through kinetic energy conservation, in: Proceedings of IEEE International Conference on Robotics and Automation, 1993, pp. 20–25.
- [25] S. V. Shah, A. Gattupalli, Energy Optimum Reactionless Path Planning for Capture of Tumbling Orbiting Objects using a Dual-Arm Robot, in: Proceedings of the 1st International and 16th National Conference on Machines and Mechanisms, 2013, pp. 16–21.
- [26] R. Lamariello, G. Hirzinger, Generating feasible trajectories for autonomous on-orbit grasping of spinning debris in a useful time, in: Proceedings of IEEE/RSJ International Conference on Intelligent Robots and Systems, 2013, pp. 5652–5659.

- [27] H. Sone, D. N. Nenchev, On some practical reactionless motion tasks with a free-floating space robot, in: Proceedings of IEEE International Conference on Robotics and Automation, 2015, pp. 2836–2841.
- [28] D. Nenchev, K. Yoshida, Impact analysis and post-impact motion control issues of a free-floating Space robot subject to a force impulse, *IEEE Transactions on Robotics and Automation* 15 (3) (1999) 548–557.
- [29] M. Oda, K. Kibe, F. Yamagata, ETS-VII, space robot in-orbit experiment satellite, in: Proceedings of IEEE International Conference on Robotics and Automation, Vol. 1, 1997, pp. 739–744.
- [30] Y. Nakamura, H. Hanafusa, T. Yoshikawa, Task-priority based redundancy control of robot manipulators, *The International Journal of Robotics Research* 6 (2) (1987) 3–15.
- [31] A. Dietrich, C. Ott, A. Albu-Schaffer, An overview of null space projections for redundant, torque-controlled robots, *The International Journal of Robotics Research* 34 (11) (2015) 1385–1400.
- [32] K. Kreutz-Delgado, M. Long, H. Seraji, Kinematic analysis of 7-DOF manipulators, *The International Journal of Robotics Research* 11 (5) (1992) 469–481.
- [33] R. Boudreau, R. Podhorodeski, Singularity analysis of a kinematically simple class of 7-jointed revolute manipulators, *Transactions of the Canadian Society for Mechanical Engineering* 34 (1) (2010) 105–117.
- [34] S. Chiaverini, B. Siciliano, O. Egeland, Review of the damped least-squares inverse kinematics with experiments on an industrial robot manipulator, *IEEE Transactions on Control Systems Technology* 2 (2) (1994) 123–134.
- [35] D. N. Nenchev, Singularity-Consistent Parameterization of Robot Motion and Control, *The International Journal of Robotics Research* 19 (2) (2000) 159–182.
- [36] S. Taki, D. Nenchev, Euler angle based feedback control of large eigenaxis rotations in the presence of singularities and model uncertainty, in: Proceedings of the 13th International Conference on Control, Automation and Systems, 2013, pp. 34–39.

- [37] S. Chiaverini, Singularity-robust task-priority redundancy resolution for real-time kinematic control of robot manipulators, *IEEE Transactions on Robotics and Automation* 13 (3) (1997) 398–410.
- [38] M. Torres, S. Dubowsky, Path-planning for elastically constrained space manipulator systems, in: *Proceedings of IEEE International Conference on Robotics and Automation*, 1993, pp. 812–817.